A&A 397, 181–189 (2003)
DOI: 10.1051/0004-6361:20021103

Astronomy & Astrophysics

Multitransitional observations of the CS core of L673

O. Morata, J. M. Girart, and R. Estalella

Departament d'Astronomia i Meteorologia, Universitat de Barcelona, Av. Diagonal, 647, 08028, Barcelona, Spain

Received 7 January 2002 / Accepted 29 July 2002

Abstract. A multitransitional study with the BIMA interferometric array was carried out toward the starless core found in the L673 region, in order to study the small-size structure of the cores detected with previous single-dish observations, which provides us with a test of the predictions of the chemical model of Taylor et al. (1996, 1998). We detected emission in the CS ($J = 2 \rightarrow 1$), N_2H^+ ($J = 1 \rightarrow 0$), and HCO^+ ($J = 1 \rightarrow 0$) lines. Several clumps of size $\lesssim$0.08 pc were found for each line distributed all over the region where previous single-dish emission was found (Morata et al. 1997). Each molecular transition traces differently the clump distribution, although in some cases the detected clumps are coincident. The distribution of the N_2H^+ emission and the single-dish NH_3 emission are coincident and compatible with an origin in the same gas. The large fraction of missing flux measured for the CS ($2 \rightarrow 1$) transition can be explained if the cloud is formed by a clumpy and heterogeneous medium. Four positions were selected to derive the abundance ratios [N_2H^+/CS] and [HCO^+/CS] from the molecular column density determinations, and to compare them with the values predicted by the chemical model. The model was able to explain the interferometric observations, and, in particular, the chemical differentiation of the detected clumps and the coincidence of the NH_3 and N_2H^+ emissions. The lack of HCO^+ towards the two selected positions that trace the more evolved clumps cannot be accounted for by the model, but it is possibly due to strong self-absorption. We propose a classification of the studied clumps according to the stage of chemical evolution indicated by the molecular abundances.

Key words. molecular processes – ISM: abundances – ISM: clouds – ISM: molecules – ISM: individual objects: L673

1. Introduction

Low-mass star formation takes place in dense cores of molecular clouds (Beichman et al. 1986; Benson & Myers 1989). The emission of several molecules, such as CS, NH_3, and HCO^+, known to be good tracers of high density molecular gas, has been used to study these dense cores. However, very soon large discrepancies between the emission of these molecules were found in some sources (Zhou et al. 1989; Myers et al. 1991). To clarify the intrinsic differences between the emission of these molecules and how this emission is related to the actual distribution of the high density gas, we began a systematic comparison between the emission of the CS ($J = 1 \rightarrow 0$) and NH_3 $(J, K) = (1, 1)$ transitions under similar conditions of angular resolution (Pastor et al. 1991; Morata et al. 1997). The comparison of the distribution of the CS and NH_3 emission in 14 condensations of 11 star-forming regions confirmed the discrepancies. In particular, we found that there is a separation ~0.2 pc between the emission peaks of both molecules; regions traced by CS are larger than those traced by NH_3; and CS lines are ~0.5 km s^{-1} wider than those of NH_3.

To explain these results, we developed a chemical model (Taylor et al. 1996) in which high density condensations, or dense cores, are formed by clumps $\lesssim$0.1 pc in size, which would be unresolved at moderate angular resolution observations such as the ones made in our study, of different mass, age, size and density. Most of the clumps disperse before NH_3 abundances build up to significant levels, though these clumps contain substantial CS, so its emission should be observable. A few clumps, those sufficiently long lived, or being in a more advanced stage of physical and chemical evolution because of being denser or more massive, form a significant content of NH_3, while CS abundance decreases with time. These clumps would possibly continue their evolution to eventually form stars. This model would account for the difference in size and separation between emission peaks of the CS and NH_3 molecules.

Our chemical model explains the differences as a result of the speed at which the molecules form. Therefore, a classification could be made between *"early-time"* molecules and *"late-time"* molecules, according to the time at which these molecules reached their peak fractional abundance. We examined whether there were other potentially observable molecules that should show extended emission like CS, or more compact emission as NH_3 (Taylor et al. 1998). Several candidates were found for both groups: e.g. HCN, H_2CO or HC_3N are found in the CS family, whilst HCO^+, SO, NO or N_2H^+ are in the NH_3 family.

In order to study the small-size structure of the cores detected with the single-dish observations, which also provides us with a test of the predictions of the chemical model, we

Send offprint requests to: O. Morata,
e-mail: oscar@am.ub.es

Table 1. Transitions observed.

Molecule	Transition	ν (GHz)	RMS per channel (Jy/beam)	Spectral resolution (km s^{-1})	Detected?
HCO^+	$1 \rightarrow 0$	89.18852	0.17	0.33	Yes
C_3S	$16 \rightarrow 15$	92.48849	0.18	0.32	No
N_2H^+	$1 \rightarrow 0$	93.17402	0.16	0.32	Yes
C_2S	$8_7 \rightarrow 7_6$	93.87010	0.18	0.31	No
OCS	$8 \rightarrow 7$	97.30121	0.22	0.30	No
CS	$2 \rightarrow 1$	97.98097	0.18	0.30	Yes
HNCS	$9_{1,8} \rightarrow 8_{1,7}$	105.74386	0.25	0.28	No
C_2S	$9_8 \rightarrow 8_7$	106.34774	0.24	0.28	No
HC_3N	$12 \rightarrow 11$	109.17363	0.26	0.27	No
SO	$2_3 \rightarrow 1_2$	109.25218	0.25	0.27	marginally
OCS	$9 \rightarrow 8$	109.46306	0.25	0.27	No

carried out high angular resolution observations towards L673 of several transitions corresponding to molecules of both families of species. The L673 high density condensation was previously detected in the CS ($J = 1 \rightarrow 0$) transition at moderate angular resolution by Morata et al. (1997). The L673 CS condensation is located at $\alpha(J2000) = 19^h20^m52\overset{s}{.}1$, $\delta(J2000) = +11°15'29\overset{''}{.}5$, at $\sim 9\overset{''}{.}5$ to the southeast of IRAS 19180+1116. This condensation is well suited to our purposes for several reasons. A high density condensation has been detected nearby in the NH_3 $(J, K) = (1, 1)$ transition by Sepúlveda et al. (2002), which shows the same general behavior found in the other sources of our survey: a separation from the CS emission peak $\sim 2'$, and a NH_3 condensation size clearly smaller than the CS condensation size. It is located nearby, the estimated distance to the L673 cloud is ~300 pc (Herbig & Jones 1983), which helps in the study of the smaller size structure of the cloud. Finally, the condensations detected in CS and NH_3 show no signs of tracers of star formation, such as infrared or radio continuum sources, Herbig-Haro objects or molecular outflows, which indicates that it is probably a quiescent core, maybe in the first stages of collapse, before forming a stellar core or a Class 0 star, and thus fulfilling the conditions of the chemical model we developed.

2. Observations

The observations of the L673 region were carried out in 1998 May with the 10-antenna BIMA array[1] at the Hat Creek Radio Observatory in the C configuration. The phase calibrators were 1751+096 and 3C395. In order to include the positions of the CS ($J = 1 \rightarrow 0$) and NH_3 $(J, K) = (1, 1)$ transitions single-dish emission peaks of the maps by Morata et al. (1997) and Sepúlveda et al. (2002), we made a two-point mosaic with each of the fields centered approximately at the position of these two peaks. Thus, one of the fields was centered at the position $\alpha(2000) = 19^h20^m52\overset{s}{.}2$, and $\delta(2000) = +11°13'57''$, and the other located $90''$ to the North. Three frequency setups were used, centered at 91, 96 and 107 GHz. The digital correlator was configured to observe simultaneously several molecular line transitions at moderately high spectral resolution, ~0.3 km s^{-1}. The target molecular lines were HCO^+ ($J = 1 \rightarrow 0$), N_2H^+ ($J = 1 \rightarrow 0$), CS ($J = 2 \rightarrow 1$), SO ($J_K = 2_3 \rightarrow 1_2$) and $C^{18}O$ ($J = 1 \rightarrow 0$). System temperatures for the 91, 96 and 107 GHz setups were in the 180–500 K, 250–700 K and 500–1000 K range, respectively. The calibration and data reduction were performed using the MIRIAD software package (Sault et al. 1995). Mosaic maps were done with the visibility data weighted by the associated system temperatures and using natural weighting, and applying the primary beam correction. The resulting synthesized beam for the 91, 96 and 107 GHz setups were $12\overset{''}{.}7 \times 9\overset{''}{.}6$, PA = −14°; $13\overset{''}{.}3 \times 10\overset{''}{.}5$, PA = −17°; and $13\overset{''}{.}1 \times 9\overset{''}{.}3$, PA = −8°, respectively. The transitions of all the observed lines, their velocity resolution and the achieved rms noise with this velocity resolution are listed in Table 1. For the continuum emission we used the data from the 96 GHz correlator setup, which provided a bandwidth of 800 MHz centered at the frequency of 95.9 GHz. No emission was detected at above 8 mJy beam^{-1} (at a 3-σ level).

3. Results

3.1. Morphology of the molecular emission

We detected emission in three of the transitions: CS ($J = 2 \rightarrow 1$), N_2H^+ ($J = 1 \rightarrow 0$), and HCO^+ ($J = 1 \rightarrow 0$). We detected marginally, at $\sim 2\sigma$ level, the SO ($2_3 \rightarrow 1_2$) transition. The remaining transitions of Table 1, which where observed mainly because they were found inside the frequency range of the observations, were not detected. It must be noted that all these undetected transitions have an upper level energy with temperatures higher than 15 K, and most of them, OCS is the exception, have also a high dipole moment. Thus, the temperature and density conditions of the L673 core, and the low abundances expected for these molecules make them very difficult to detect.

Figures 1 to 3 show the maps of the zero-order moment (integrated intensity) of the emission of the detected molecules.

[1] The BIMA array is operated by the Berkeley-Illinois-Maryland Association with support from the National Science Foundation.

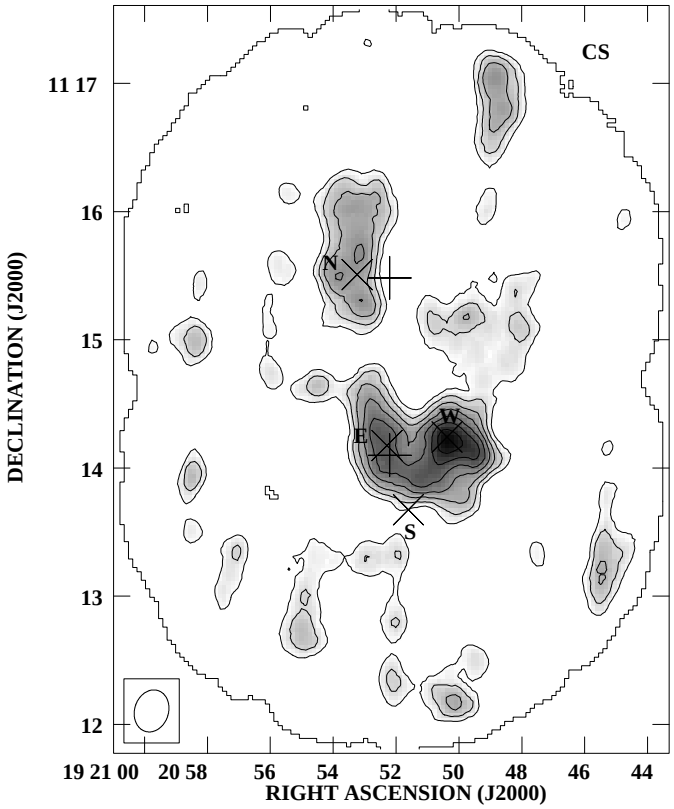

Fig. 1. Integrated emission of the CS ($J = 2 \rightarrow 1$) line for the $V_{\rm LSR}$ range 5.6–9.8 km s^{-1}. Contours are 0.96, 1.20, 1.44, 1.68, 1.92, 2.16, 2.40, 2.64 Jy beam^{-1} km s^{-1}. The beam ($20'' \times 15\farcs8$) is shown in the bottom left-hand corner. The upright crosses indicate the nominal position of the single-dish emission peak of the CS ($J = 1 \rightarrow 0$) line (north) and NH_3 (J, K) = (1, 1) line (south). The tilted crosses indicate the position of the four points selected for further study (see Table 2). The bordering contour indicates the two fields observed.

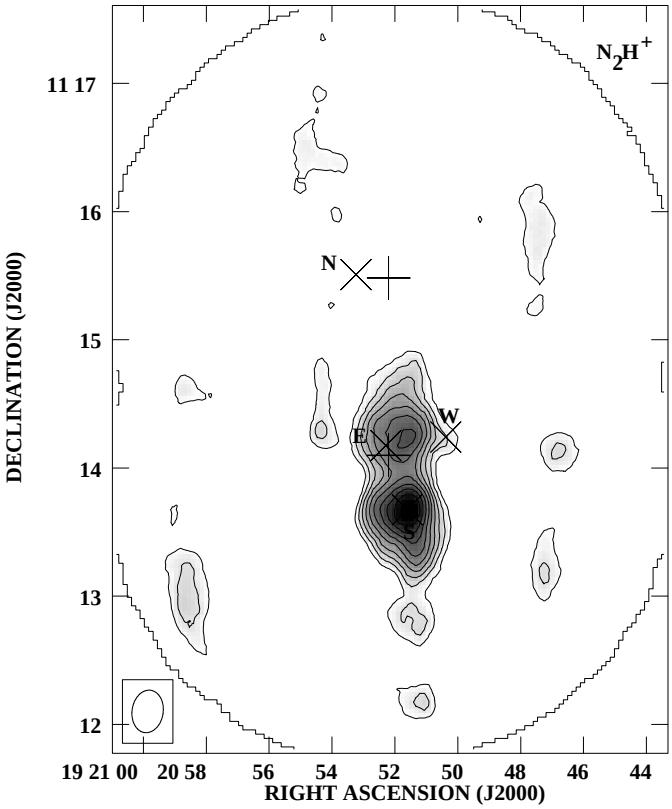

Fig. 2. Same as in Fig. 1 for the N_2H^+ ($J = 1 \rightarrow 0$) line for the V_{LSR} range −1.4–14.2 km s^{-1}. Contours are 2.55, 3.06, 3.57, 4.08, 4.59, 5.10, 5.61, 6.12, 6.63, 7.14 Jy beam^{-1} km s^{-1}. The beam ($20'' \times 14\farcs6$) is shown in the bottom left-hand corner.

These maps were obtained after convolving the original maps with a Gaussian function, with a resulting beam of $\sim 20'' \times 15''$, in order to make a more meaningful comparison between the emission of each molecule.

A clumpy distribution of the emission is shown in the integrated intensity map of the CS ($J = 2 \rightarrow 1$) transition (Fig. 1). The more intense emission is found in two clumps near the position of the single-dish NH_3 (J, K) = (1, 1) emission peak: one almost coinciding with its nominal position, and the other peaking $\sim 30''$ to the west. Weaker emission is found in a clump near the position of the single-dish CS ($J = 1 \rightarrow 0$) emission maximum, $\sim 1\farcm5$ to the north.

Figure 2 shows the integrated intensity map of N_2H^+ ($J = 1 \rightarrow 0$). Two clumps of emission are found, one almost coincident with the nominal position of the NH_3 (J, K) = (1, 1) emission peak, and the other, more intense, $\sim 0\farcm6$ to the south. No emission is detected around the position of the CS ($J = 1 \rightarrow 0$) single dish emission peak.

The integrated intensity map of the HCO^+ ($J = 1 \rightarrow 0$) emission (Fig. 3) shows several isolated emission enhancements distributed around the positions of the CS and NH_3 single-dish emission peaks. The most intense emission tends to be around the position of the CS ($J = 1 \rightarrow 0$) emission peak or in-between the two peaks, with a N–S elongation. Another intense enhancement is found $\sim 1\farcm1$ south-east of the NH_3 emission peak nominal position.

Comparing the integrated intensity maps of the three molecules, we found that N_2H^+ emission was more concentrated than CS and HCO^+ emission, which were found more spread all over the region. CS ($J = 2 \rightarrow 1$) emission in the southern region coincided with the northern clump of N_2H^+ emission. Moreover, the northern N_2H^+ emission peak was found between the two CS ($J = 2 \rightarrow 1$) local emission enhancements. CS ($J = 2 \rightarrow 1$) and HCO^+ emission were found to coincide closely at the northern part of the region, especially around the CS ($J = 1 \rightarrow 0$) emission peak. On the contrary, N_2H^+ and HCO^+ emission coincided only marginally in general. Finally, we were also able to find an emission enhancement in the marginally detected SO emission very near the position of the N_2H^+ northern clump.

Table 2 lists the four positions we selected in the mapped region in order to compare the physical parameters of the gas traced by each molecule. The selected positions were related to the most prominent higher resolution clumps found in our observations, and corresponded to local intensity peaks in the emission of the detected molecules. The four positions were labeled as S, E, W and N, and roughly correspond to the South peak position of the N_2H^+ integrated intensity map, the East CS local maximum, the West CS maximum, and the North

Table 2. Selected positions.

	Position		map counterpart
	α (J2000)	δ (J2000)	
South (S)	$19^h20^m51.61^s$	$11°13'40''.5$	N_2H^+ ($J = 1 \rightarrow 0$) south peak
East (E)	$19^h20^m52.29^s$	$11°14'10''.5$	CS ($J = 2 \rightarrow 1$) eastern peak
West (W)	$19^h20^m50.38^s$	$11°14'14''.5$	CS ($J = 2 \rightarrow 1$) western peak
North (N)	$19^h20^m53.24^s$	$11°15'30''.5$	HCO^+ ($J = 1 \rightarrow 0$) NE enhancement

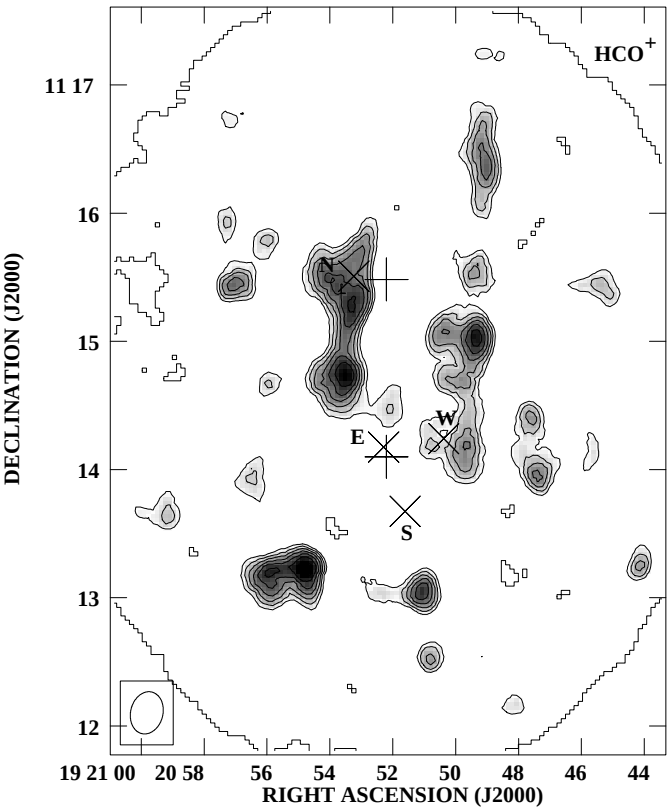

Fig. 3. Same as in Fig. 1 for the HCO^+ ($J = 1 \rightarrow 0$) line for the V_{LSR} range 5.6–9.8 km s^{-1}. Contours are 0.96, 1.08, 1.20, 1.32, 1.44, 1.56, 1.68 Jy beam^{-1} km s^{-1}. The beam ($20'' \times 15''.1$) is shown in the bottom left-hand corner.

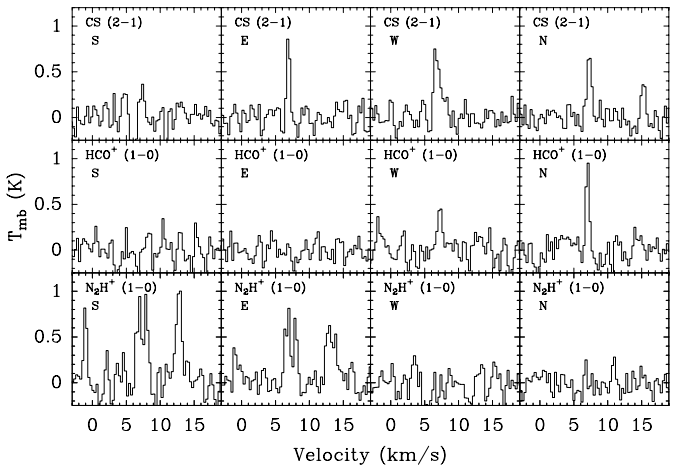

Fig. 4. Spectra of the CS ($J = 2 \rightarrow 1$), HCO^+ ($J = 1 \rightarrow 0$), and N_2H^+ ($J = 1 \rightarrow 0$) transitions at the four selected positions in our mapped region.

enhancement in the HCO^+ emission near the CS ($J = 1 \rightarrow 0$) emission peak, respectively.

3.2. Kinematic structure

Figure 4 shows the spectra obtained for the three transitions detected in the region in the four selected points. Table 3 lists the fitted line parameters for each detected transition. CS emission is detected, with varying intensity, in all four positions, whereas HCO^+ emission is only detected at the N and W positions, and N_2H^+ emission at the S and E positions. Line center velocities for CS and HCO^+ at the positions where a reliable fit could be obtained are compatible with being originated in the same bulk of gas. The difference in the line center velocity is ∼0.3–0.5 km s^{-1}, which is the velocity resolution of our observations. However, line center velocities for the N_2H^+ spectra were shifted >0.7 km s^{-1} from the CS line velocities. Using the much better determined frequency for the main N_2H^+ ($J = 1 \rightarrow 0$) component ($F_1, F = 2, 3 \rightarrow 1, 2$) given by Caselli et al. (1995): 93.17378 GHz, we found a good agreement with CS spectra line velocities, ≲0.3 km s^{-1}. We have corrected the N_2H^+ line velocities accordingly, as Table 3 shows. Linewidths are <0.8 km s^{-1}, very similar to the observed values in the single-dish observations, except for the W clump where velocity dispersion is higher, ∼1.0 km s^{-1}.

3.3. Physical parameters

We were able to estimate the excitation temperature for the N_2H^+ data at the two positions, S and E, where we had good signal-to-noise spectra. The values obtained at both positions are ∼4 K (assuming a beam filling factor $f = 1$), which is compatible with the value obtained from the CS ($J = 1 \rightarrow 0$) observations, 4.2 K (Morata et al. 1997), and slightly lower than the value obtained from the NH_3 $(J, K) = (1, 1)$ observations, 5.7 K (Sepúlveda et al. 2002). The total line opacity of the N_2H^+ ($J = 1 \rightarrow 0$) transition at both positions is ∼1.0. We estimated an upper limit for the beam averaged column density using the value for the excitation temperature obtained from the CS ($J = 1 \rightarrow 0$) and N_2H^+ ($J = 1 \rightarrow 0$) observations, $T_{ex} = 4$ K, and assuming a filling-factor $f = 1$. However, the filling-factor could be $f < 1$. In this case, the excitation temperature would be greater than 4 K, but likely less than 10 K,

Table 3. CS ($J = 2 \rightarrow 1$), HCO^+ ($J = 1 \rightarrow 0$), and N_2H^+ ($J = 1 \rightarrow 0$) lines and physical parameters obtained at the four selected positions in our region.

Molecule & Transition	Pos.	$T_{\rm mb}$ (K)	$A\tau_m$ [a] (K)	$V_{\rm LSR}$ (km s^{-1})	ΔV (km s^{-1})	τ_m [b]	τ	$N_{\rm mb}$ [c] (10^{11} cm^{-2})
CS	S	0.35 ± 0.12		$+7.4 \pm 0.1$	0.7 ± 0.2		0.05–0.4 [d]	12.0–26.9
(J=2→1)	E	0.96 ± 0.11		$+6.9 \pm 0.1$	0.5 ± 0.1		0.15–2.1 [d]	25.3–84.8
	W	0.73 ± 0.10		$+6.8 \pm 0.1$	1.0 ± 0.1		0.11–1.1 [d]	37.2–99.6
	N	0.72 ± 0.11		$+7.3 \pm 0.1$	0.8 ± 0.1		0.11–1.1 [d]	27.1–72.2
HCO^+	S	< 0.37 [e]		–	–		< 0.39 [d]	< 4.73
(J=1→0)	E	< 0.29 [e]		–	–		< 0.29 [d]	< 3.60
	W	0.48 ± 0.13		$+7.2 \pm 0.1$	0.8 ± 0.3		0.07–0.6 [d]	4.7–7.7
	N	1.02 ± 0.12		$+7.0 \pm 0.1$	0.6 ± 0.1		0.16–2.3 [d]	7.7–19.1
N_2H^+	S		0.32 ± 0.05	$+7.0 \pm 0.1$	0.5 ± 0.1 [f]	0.25 ± 0.10	1.0 [g]	2.2–3.1
(J=1→0)	E		0.24 ± 0.04	$+7.0 \pm 0.1$	0.5 ± 0.1 [f]	0.27 ± 0.10	1.0 [g]	1.7–2.4
	W		< 0.20 [e]	–	–	–	< 0.7 [d]	< 2.0
	N		< 0.16 [e]	–	–	–	< 0.5 [d]	< 1.6

[a] Derived from the transfer equation, where $A = f[J(T_{\rm ex}) - J(T_{\rm bg})]$ is the "amplitude" (Pauls et al. 1983), f is the filling factor, $T_{\rm ex}$ the excitation temperature of the transition, $T_{\rm bg}$ the background radiation temperature, and $J(T)$ the intensity in units of temperature.

[b] Optical depth of the main line.

[c] Beam averaged column density calculated from

$$N_{\rm mb} = fN = \frac{3k}{4\pi^3 \nu \mu_D^2} \frac{T_{\rm ex} + \frac{h\nu}{6Jk}}{\exp[-h\nu(J-1)/2kT_{\rm ex}] - \exp[-h\nu(J+1)/2kT_{\rm ex}]} \frac{1}{J(T_{\rm ex}) - J(T_{\rm bg})} \int T_{\rm mb} dV$$

where f is the beam filling factor, μ_D the dipole moment of the molecule, J the lower level of the transition, and $J(T)$ the intensity in units of temperature.

[d] Derived from the transfer equation, assuming for the excitation temperature upper and lower values of 10 K and 4 K, respectively.

[e] Upper limit taken as 3σ, where σ is the sensitivity per channel.

[f] Intrinsic line width

[g] Total line opacity

because the kinetic temperature in low-mass dense cores is typically about 10 K, and the excitation temperature will not be greater than this value. Thus, we used an upper value for the excitation temperature $T_{\rm ex} = 10$ K, which implies a lower limit for the beam average column density. The values for the line opacity, τ, and the beam averaged column density, $N_{\rm mb}$ for the four selected positions are shown in Table 3.

3.4. Comparison with single-dish observations

We compared the CS ($J = 2 \rightarrow 1$) interferometric and ($J = 1 \rightarrow 0$) single-dish emissions. Figure 5 shows the single-dish CS ($J = 1 \rightarrow 0$) spectra obtained at the positions of the CS ($J = 1 \rightarrow 0$) and NH_3 $(J, K) = (1, 1)$ emission peaks, compared with the BIMA CS ($J = 2 \rightarrow 1$) spectra obtained at the same positions after convolving the data with a Gaussian function to obtain a 1.′9 resulting beam, equal to the beamsize of the single-dish observations. Line center velocities agree within 0.3 km s^{-1}, our spectral resolution in both sets of observations. Line widths are almost coincident at the southern position, while the ($J = 1 \rightarrow 0$) line is ∼0.35 km s^{-1} wider at the northern position. In order to estimate the flux loss in our interferometric observations, we calculated the line intensity we should obtain for the ($J = 2 \rightarrow 1$) line from the ($J = 1 \rightarrow 0$) line opacity and excitation temperature obtained previously in the single-dish observations (Morata et al. 1997). We found that the measured line intensity is ∼8% in the northern position, and ∼12% in the south position from the estimated values. These results are compatible with the characteristics of the BIMA array, which is insensitive to structures larger than about 10 times the synthesized beamwidth (Wright 1996), which in our case is ∼1.′5–2′ (0.13–0.17 pc), of the order of the single-dish beamsize.

However, the existence of such an extended component, responsible for ∼90% of the single-dish line intensity, would not affect significantly the beam averaged column densities determined from our interferometric observations. Assuming a size of 120″ for the extended component, its contribution to the beam averaged column density for a beam size of 17″ would be of the order of $90\% \times (17''/120'')^2 = 2\%$. Thus, the beam averaged column densities determined from our observations are not significantly affected by the missing emission by the BIMA interferometer, assuming that it is due to an extended cloud component.

Figure 6 shows the distribution of the single-dish CS ($J = 1 \rightarrow 0$) (Morata et al. 1997) and NH_3 $(J, K) = (1, 1)$ (Sepúlveda et al. 2002) emission in the same region mapped by the interferometric observations. We found that most of the strongest CS ($J = 2 \rightarrow 1$) emission and particularly all the

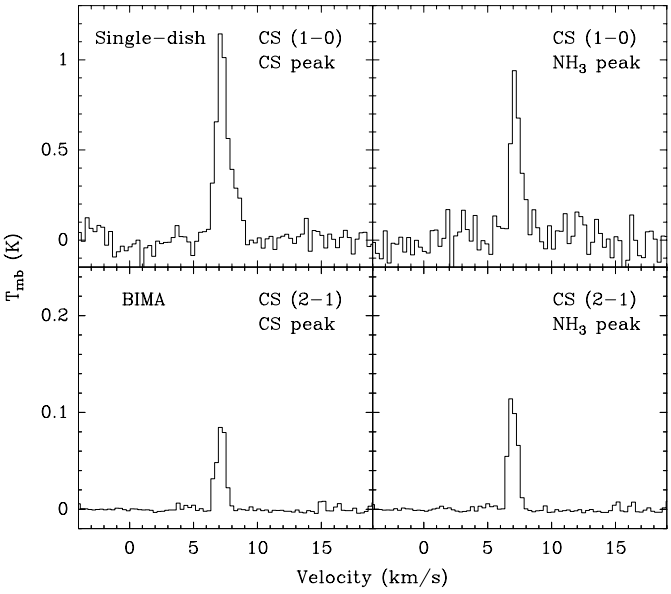

Fig. 5. Spectra of the CS ($J = 1 \rightarrow 0$) transitions obtained at the positions of the CS ($J = 1 \rightarrow 0$) and NH_3 (J, K) = (1, 1) single-dish emission peaks with the Yebes telescope (top), compared with the spectra of the CS ($J = 2 \rightarrow 1$) transition obtained at the same positions after convolving the BIMA data with a beam of 1.′9 equal to the single-dish beam (bottom). Note the different vertical scales.

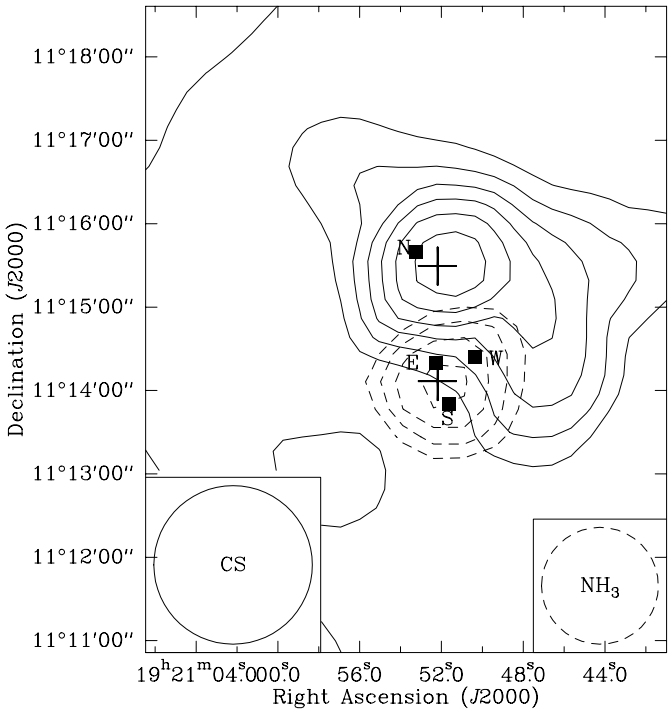

Fig. 6. Contour map of the single-dish integrated line intensity of the CS ($J = 1 \rightarrow 0$) line (solid line) obtained with the Yebes telescope (Morata et al. 1997), and the single-dish main beam brightness temperature of the NH_3 (J, K) = (1, 1) transition (dashed line) obtained with the Haystack telescope (Sepúlveda et al. 2002). The lowest CS contour level is 0.48 K km s^{-1}, and the increment is 0.05 K km s^{-1}. The lowest NH_3 contour level is 1.35 K, and the increment is 0.3 K. The crosses indicate the nominal position of the single-dish emission peaks of the CS ($J = 1 \rightarrow 0$) line (north) and NH_3 (J, K) = (1, 1) line (south). The filled squares indicate the position of the four points selected for further study in the interferometric observations.

detected N_2H^+ emission were enclosed inside the half-maximum contours of the NH_3 map, located at the southern region of the map. All four relative emission enhancements in these two transitions are also enclosed inside the beam of the single-dish observations. HCO^+ emission was fainter around this southern region, and marginal in the eastern, western and southern margins of the NH_3 intensity contours. Around the northern region, no N_2H^+ emission was detected, but CS and HCO^+ emission were enclosed by the beam of the CS single-dish observations. Emission around this position was not as concentrated as around the southern region, but we found intense HCO^+ and CS ($J = 2 \rightarrow 1$) emission very near the beam center.

4. Discussion

4.1. Structure of the core

The integrated intensity maps of the CS ($J = 2 \rightarrow 1$), N_2H^+ ($J = 1 \rightarrow 0$), and HCO^+ ($J = 1 \rightarrow 0$) transitions obtained with the BIMA interferometer showed that a much clumpier medium is revealed by the high angular resolution observations than by the single-dish maps of CS ($J = 1 \rightarrow 0$) (Morata et al. 1997) and NH_3 (J, K) = (1, 1) (Sepúlveda et al. 2002) obtained with an angular resolution of ∼1.′5. Several clumps of size ≲0.08 pc are found distributed all over the region where the strongest emission of the single-dish observations was located, which would support the idea that at least part of the single-dish emission was originated in clumps of smaller size, <0.1 pc (Taylor et al. 1996). Moreover, these small size clumps, although coinciding in some cases, are traced differently by each molecule, which would support the idea of a chemical differentiation between each clump of gas depending on the local density and age. However, we found that ∼90% of the single-dish CS emission is not detected by the interferometric observations. As we have already pointed out, the BIMA array is insensitive to structures larger than ∼0.17 pc, which could mean that part of the emission could come from chemically young clumps of that size or larger, undetectable then by BIMA, but whose emission was detected by the single-dish observations. Another possibility is that there could also be clumps smaller than the ones we found, of low density, and with emission not strong enough to be detected with the interferometer.

In order to qualitatively test which of the aforementioned two possibilities is more consistent with our observations, we modeled the filtering effect of the BIMA interferometer response to a molecular core with an homogeneous and extended geometry and a clumpy heterogeneous geometry. The process of generating synthetic visibility data matching that expected from true observations with the BIMA interferometer was performed by using the MIRIAD task UVGEN. This process is described by Girart & Acord (2001). Our synthetic observations had the same phase center as the L673 observations and were done for the BIMA C-array configuration. The total flux

adopted for both cases, the extended and clumpy structures, was similar to that expected for the CS ($J = 2 \rightarrow 1$) transition, calculated from the measured CS ($J = 1 \rightarrow 0$) intensity. The results obtained were:

1. *Extended and homogeneous medium.* The presence of the extended emission was modeled as single large component. We tested the filtering effect of the interferometer for different sizes and different center positions of the cloud with respect to the phase center. We found that in order to achieve a missing flux of about 90%, the value estimated for the BIMA observations, large sizes were required: diameter $\gtrsim 2'$. The resulting synthetic maps showed strong negative lobes extending ~40″ along the N–S direction, at both sides of the center of the synthetic cloud. This was due to a combination of the effects of source structure, with a large fraction of undetected flux by the interferometer, and visibility coverage of the BIMA interferometer for a source of low declination ($\delta = 11^\circ$ for L673). These negative structures could not be removed in the cleaning process. The cleaned maps had absolute peak intensities of the negative structures with similar, or even higher, values than the positive structures.
   However the real BIMA CS ($J = 2 \rightarrow 1$) channel maps does not show such strong negative structures. At the central velocities of the CS line there are some negative lobes, but their intensity is only a $\lesssim$40% of the positive peaks.
2. *Clumpy and heterogeneous medium.* The chemical models of Taylor et al. (1996, 1998) assume that the clouds are formed by clumps of $\lesssim$0.1 pc with different sizes, ages and masses. From this assumption it is expected a cloud formed with only few massive clumps and several clumps less massive. So, we adopted a simplistic model of a cloud formed with one massive, thereby strong, clump and between 15 and 20 less massive, thereby weaker, clumps. We found that even most of the emitting flux came from the smaller clumps, the BIMA synthetic resulting maps were clearly dominated by the strongest clump, and a large fraction of the emission from the weaker clumps was undetected by the interferometer. In some of the cases modeled, the total missing flux was of ~80% of the total flux. The residual negative structures of the synthetic maps were 30–50% of the positive.

In summary, without going to an exhaustive analysis of the response of the BIMA interferometer to the different cloud structures, we find that in L673 the missing flux is most probably due to a clumpy heterogeneous structure.

4.2. Chemical abundances

In our maps, we found that all the detected N_2H^+ emission was enclosed inside the half-maximum contours of the NH_3 map of Sepúlveda et al. (2002), with the strongest N_2H^+ emission found inside the highest NH_3 contours. The nominal position of the NH_3 emission peak is placed between the two local N_2H^+ emission peaks, although the beam enclosed both maxima. The chemical model developed by Taylor et al. (1996, 1998) marks the NH_3 and N_2H^+ molecules as forming at late times, when sufficiently high densities are reached or in long lived clumps. Thus, they should be found in the same region. The coincidence between the distribution of the emission of N_2H^+ observed by the BIMA interferometer and the NH_3 emission detected by single-dish observations, and the overall morphological appearance of the NH_3 and N_2H^+ emission seem to support these predictions. Moreover, both interferometric and single-dish emissions are highly concentrated, and are compatible with being originated in the same gas since the emission of N_2H^+ could be coming from two clumps of size ~0.′6 × 1′ enclosed inside the higher levels of the lower resolution emission of NH_3. The SO molecule was also marked in our model as a late-time molecule. The near coincidence of the clump found in the marginally detected SO emission with the northern clump of the N_2H^+ emission would support that classification.

Table 4. Column density ratios.

Position	$[HCO^+/CS]$	$[N_2H^+/CS]$	$N(CS)/N_{max}(CS)$
S	<0.21	0.15	30%
E	<0.07	0.05	77%
W	0.10	<0.02	100%
N	0.27	<0.02	73%

Table 4 shows the column density ratios of N_2H^+ and HCO^+ over CS for the four selected positions calculated from the column density determinations of Table 3, and the CS column density relative to the maximum value, found in position W. We observe that N_2H^+ abundance is ~5–15% of that of CS for the S and E positions, and becomes lower at the N and W positions. $[HCO^+/CS]$ is $\lesssim$20% for the S, E, and W positions, and becomes ~30% at the N position, while there is a factor 3 variation in the CS column density. We can then differentiate between the N and W positions, where HCO^+ is clearly detected while N_2H^+ is not, and the E and S positions where N_2H^+ is clearly detected whereas HCO^+ is not detected.

4.3. Modeling the chemical evolution

We used the results of the model explained in Taylor et al. (1998) to compare the predicted abundances of HCO^+ and N_2H^+ with respect to CS, with the values we obtained for the column density ratios, and see if some chemical age determination could be made for these positions. Figure 7 shows the predicted fractional abundances for several molecules of interest for values of collapse, $B = 1$, freeze-out, FR = 0.01, and final density $n_f = 5 \times 10^4$ cm^{-3} (see Taylor et al. 1996, 1998). We also show the molecular abundance relative to CS for the HCO^+, N_2H^+, and NH_3 molecules.

We found that the abundance $[HCO^+/CS]$ can be explained by the model in relatively short times, between $2–3 \times 10^6$ years. Thus, a higher HCO^+ fractional abundance would indicate a more chemically evolved clump. However, this does not seem to agree with the abundance of N_2H^+. First, N_2H^+ reaches high abundances at later times, and one would expect to find N_2H^+ at more evolved clumps. Second, the model can not explain fractional abundances of N_2H^+ similar to those of HCO^+, and as high as those we found in the S and E positions.

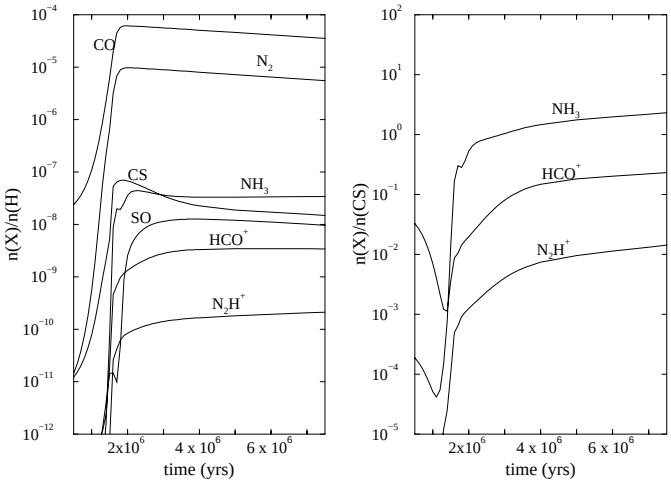

Fig. 7. *Left panel*: Chemical fractional abundances (relative to H nuclei) as a function of time for a free-fall collapse model halted at density $n_{\rm H} = 5 \times 10^4$ cm^{-3}. Initially $n_{\rm H} = 1 \times 10^3$ cm^{-3} and $A_V = 0.5$. Freeze-out parameter $FR = 0.01$, corresponding to an average value of the product of the dust to gas number density ratio and square of the grain radius $\langle n_{\rm d} a^2 \rangle = 2 \times 10^{-20}$ cm^{-2}. *Right panel*: Fractional abundances of selected species (relative to CS) as a function of time.

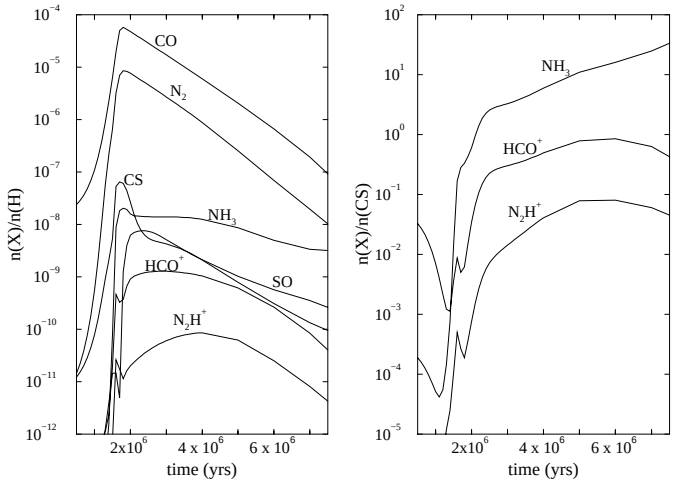

Fig. 8. *Left panel*: Chemical fractional abundances (relative to H nuclei) as a function of time for a free-fall collapse model halted at density $n_{\rm H} = 5 \times 10^5$ cm^{-3}. Initially $n_{\rm H} = 1 \times 10^3$ cm^{-3} and $A_V = 0.5$. Freeze-out parameter FR = 0.01, corresponding to an average value of the product of the dust to gas number density ratio and square of the grain radius $\langle n_{\rm d} a^2 \rangle = 2 \times 10^{-20}$ cm^{-2}. *Right panel*: Fractional abundances of selected species (relative to CS) as a function of time.

A slightly higher freeze-out parameter would provide higher relative N_2H^+ abundance with respect to CS, while not changing appreciably the fractional abundance, because CS is frozen-out to grains faster. In this case, we also obtain higher HCO^+ relative abundances with CS.

Figure 8 shows the results of the model modifying the final density value to 10 times the previous value, $n_{\rm f} = 5 \times 10^5$ cm^{-3}, and maintaining unchanged the values of B and FR. We find some differences with the previous results. CS maximum fractional abundance is similar to the previous model, while NH_3, HCO^+, and N_2H^+ reach slightly lower abundances. In any case, CS and NH_3 show the same behavior found in the model of Taylor et al. (1996). However, the higher final density produces a faster depletion of molecules, especially CS which has a steeper decline with time.

At times $\sim 2.5 \times 10^6$ years, when CS has a high fractional abundance, and HCO^+ has barely reached its maximum fractional abundance, we find a relative abundance [HCO^+/CS] $\sim$ 0.1, while N_2H^+ has still a low abundance. This could correspond to the W position of our map. At a later time, $\sim 3 \times 10^6$ years, when N_2H^+ is still at low abundances, HCO^+ abundance is practically the same while CS abundance is slightly lower, with a resulting higher [HCO^+/CS] ratio. This could correspond to the N position. At the time N_2H^+ reaches its peak abundance, $\sim 4 \times 10^6$ years, HCO^+ has diminished in abundance although it can still be observed. This would point to the S and E positions being at later stages of chemical evolution. Distinguishing between the two is difficult. The S position could be more evolved since it shows a lower CS column density, and a higher [N_2H^+/CS] ratio, which could correspond to the stage where N_2H^+ is at higher abundances.

However, even the modified model is not able to explain the observed HCO^+ low abundances obtained at positions S and E with respect to the predicted values. The HCO^+ molecule has a high dipole moment, and it has been found that the ($J = 1 \rightarrow 0$) transition line profiles are often self-absorbed in typical molecular cloud cores by foreground gas at lower density and temperature. The apparently sudden lack of HCO^+ emission in those places where N_2H^+ or CS emission is intense may suggest that the HCO^+ ($J = 1 \rightarrow 0$) emission arising from the core might be absorbed efficiently by a cold low-density envelope around the core or a foreground cloud, as in the case of the NGC 2264G region (Girart et al. 2000).

4.4. Comparison with other studies

Studies of chemical evolution have been made up to now with single-dish observations using several transitions of selected early- and late-time molecules, usually CS, N_2H^+, NH_3, HCO^+, SO, SO_2, and HC_3N. These studies of starless cores show maps where emission seems to originate in several clumps distributed all over the region (Dickens et al. 2000) or in round-like clumps (Tafalla et al. 2002). All these studies show evidences of chemical differentiation. Dickens et al. find that early- and late-time molecules are found at different positions and show differing behavior, i.e. early-time molecules are most abundant where late-time molecules are not, and viceversa. The authors explain their results invoking a difference in the chemical ages of different parts of their region. Tafalla et al. also find that their maps show a great coincidence between the emission of the N_2H^+ and NH_3 molecules, while differing from the CS emission.

Some of these studies also find evidence for differing depletion rates of molecules such as CS or NH_3. Tafalla et al. find a central abundance drop of CS, a constant abundance of N_2H^+, and a central enhancement of NH_3 in their regions, while Bergin et al. (2001), in observations of the IC 5146 cloud, also detect molecular depletion of CS, while N_2H^+ remains in

the gas phase with growing extinction. Other numerical calculations, such as Aikawa et al. (2001) also predict a depletion of certain species from the central regions. In our model, we would expect to find the more massive and chemically older clumps in the central regions. These clumps would have substantial quantities of NH_3 and N_2H^+, while CS would have been depleted from the gas phase, which would show as a central depletion of CS.

Thus, these results suggest that although our interferometric observations lose information on the total emission of the region, they are in agreement with the results obtained with single-dish telescopes, suggesting that interferometric observations are useful to study with high angular resolution the chemical evolution of inner structures of starless cores.

5. Summary

We made a multitransitional study with the BIMA interferometric array of the starless core found in the L673 (Morata et al. 1997), in order to test the chemical model of Taylor et al. (1996, 1998). The main results were:

1. We detected emission in the CS($J = 2 \rightarrow 1$), N_2H^+ ($J = 1 \rightarrow 0$), and HCO^+ ($J = 1 \rightarrow 0$) lines. We marginally detected emission in the SO ($J_K = 2_3 \rightarrow 1_2$) line.
2. The high angular resolution interferometric observations revealed a much clumpier medium than the lower resolution single-dish observations. Several clumps of size $\lesssim$0.08 pc were found for each line distributed all over the region where the single-dish emission was found.
3. Each molecular transition traced differently the clump distribution, although in some cases the detected clumps were coincident. We found that the distribution of the N_2H^+ emission was completely enclosed by the half-maximum contours of the NH_3 maps of Sepúlveda et al. (2002), and that both emissions were highly compact and compatible with being originated in the same gas. We also found a marginal coincidence with the SO molecule, which is also a late-time molecule.
4. The BIMA interferometer detected only 9–12% of the CS (2→1) emission. Modelling the filtering effect of BIMA, we found that a clumpy and heterogeneous medium could explain this effect.
5. We estimated the abundance ratios [N_2H^+/CS] and [HCO^+/CS] from the molecular column density determinations in four selected positions, labeled as S, E, W, and N, in order to compare them with the predicted values of the chemical model. We found that at the N and W positions there was a high HCO^+ abundance relative to CS and a low N_2H^+ abundance, while at the S and E positions the case was reversed.
6. The chemical model was able to explain the abundance ratios of [HCO^+/CS] at the positions where HCO^+ was detected, N and W. The best fit was for a model with a density at which collapse is halted of $n_f = 5 \times 10^5$ cm^{-3}. In this case, we found that the predicted [N_2H^+/CS] abundance ratios were more in agreement with the observations. A high HCO^+ abundance, but a low N_2H^+ abundance would represent an earlier stage, where the W and N positions could be found. The S and E positions would be in a later chemical stage on account of the higher N_2H^+ abundance, although a more precise differentiation is hard to make.

Thus, the model described in Taylor et al. (1996, 1998) applied to a starless core with no apparent signs of other star formation tracers, such as molecular outflows or radio continuum sources, was able to explain the interferometric observations, if we take into account the likely self-absorption of HCO^+. In particular, the chemical differentiation of the detected clumps and the coincidence of the NH_3 and N_2H^+ emissions agree with the model. It also enabled us to explain the HCO^+ and N_2H^+ emissions and to propose a classification of the studied clumps according to the stage of chemical evolution indicated by the molecular abundances.

Further multitransitional observations with higher sensitivity would be necessary in order to determine with more detail the physical structure of the region and to provide more data with which to refine the chemical model predictions. In particular, the observation of molecules such as H_2CO and SO, or of the isotope $H^{13}CO^+$, would help to clarify the nature of the HCO^+ ($J = 1 \rightarrow 0$) emission.

Acknowledgements. JMG acknowledges support by NSF grant AST-99-81363 and by RED-2000 from the Generalitat de Catalunya. RE and JMG are partially supported by DGICYT grant PB98-0670 (Spain). We thank the referee for the comments and discussion.

References

Aikawa, Y., Ohashi, N., Inutsuka, S.-I., Herbst, E., & Takakuwa, S. 2001, ApJ, 552, 639
Beichman, C. A., Myers, P. C., Emerson, J. P., et al. 1986, ApJ, 307, 337
Benson, P. J., & Myers, P. C. 1989, ApJSS, 71, 89
Bergin, E. A., Ciardi, D. R., Lada, C. J., Alves, J., & Lada, E. A. 2001, ApJ, 557, 209
Caselli, R., Myers, P. C., & Thaddeus, P. 1995, ApJ, 455, L77
Dickens, J. E., Irvine, W. M., Snell, R. L., et al. 2000, ApJ, 542, 870
Girart, J. M., & Acord, J. M. P. 2001, ApJ, 552, L63
Girart, J. M., Estalella, R., Ho, P. T. P., & Rudolph, A. L. 2000, ApJ, 539, 763
Herbig, G. H., & Jones, B. F. 1983, AJ, 88, 1040
Morata, O., Estalella, R., López, R., & Planesas, P. 1997, MNRAS, 292, 120
Myers, P. C., Fuller, G. A., Goodman, A. A., & Benson, P. J. 1991, ApJ, 376, 561
Pastor, J., Estalella, R., López, R., et al. 1991, A&A, 252, 320
Pauls, T. A., Wilson, T. L., Bieging, J. H., & Martin, R. N. 1983, A&A, 123, 23
Sault, R. J., Teuben, P. J., & Wright, M. C. H. 1995, in Astronomical Data Analysis Software and Systems IV, ed. R. A. Shaw, H. E. Payne, & J. J. Hayes (San Francisco: Astronomical Society of the Pacific), ASP Conf. Ser. 77, 433
Sepúlveda, I., et al. 2002, in preparation
Tafalla, M., Myers, P. C., Caselli, P., Walmsley, C. M., & Comito, C. 2002, ApJ, 569, 815
Taylor, S. D., Morata, O., & Williams, D. A. 1996, A&A, 313, 269
Taylor, S. D., Morata, O., & Williams, D. A. 1998, A&A, 336, 309
Wright, M. C. H. 1996, BIMA memo 45
Zhou, S., Wu, Y., Evans, N. J., Fuller, G. A., & Myers, P. C. 1989, ApJ, 346, 168